# A statistical analysis of the occurrence of polar stratospheric ice clouds based on MIPAS satellite observations and the ERA5 reanalysis

Ling Zou[1,3], Reinhold Spang[2,3], Sabine Griessbach[1,3], Lars Hoffmann[1,3], Farahnaz Khosrawi[1,3], Rolf Müller[2,3], and Ines Tritscher[2,3]

[1]Jülich Supercomputing Centre (JSC), Forschungszentrum Jülich, Jülich, Germany
[2]Institute of Energy and Climate Research (IEK-7), Forschungszentrum Jülich, Jülich, Germany
[3]Center for Advanced Simulation and Analytics (CASA), Forschungszentrum Jülich, Jülich, Germany

**Correspondence:** Ling Zou (l.zou@fz-juelich.de), Lars Hoffmann (l.hoffmann@fz-juelich.de)

**Abstract.** Small-scale temperature fluctuations can play a crucial role in the occurrence of ice clouds. This study analyzes a decade of ice polar stratospheric clouds (PSCs) occurrence obtained from Michelson Interferometer for Passive Atmospheric Sounding (MIPAS/Envisat) measurements. The points with the smallest temperature difference ($\Delta T_{ice\_min}$) between the frost point temperature ($T_{ice}$) and the environmental temperature along the limb line of sight are proposed here to identify the location

5 of ice PSC observations. In MIPAS observations, we find approximately 56 % of the Arctic and 28 % of the Antarctic ice PSCs are detected at temperatures above the local $T_{ice}$ based on ERA5 data at $\Delta T_{ice\_min}$. Ice PSCs above $T_{ice}$ are concentrated around mountain regions and their downwind directions. A backward trajectory analysis deduced from ERA5 reanalysis is performed to investigate the temperature history of each ice PSC observation. Based on 24-hour backward trajectories, the cumulative fraction of ice PSCs above $T_{ice}$ increases as the trajectory gets closer to the observation point. The most significant change of

10 the fraction of ice PSCs above $T_{ice}$ occurs within the 6 h preceding the observations. There is an impact of previous temperature fluctuations on the interpretation of MIPAS ice PSC observations. At the observation point, the mean fractions of ice PSCs above $T_{ice}$ taking into account temperature fluctuations along the backward trajectory are 33 % in the Arctic and 9 % in the Antarctic. The results provide quantitative assessments of the correlation between orographic waves with ice PSCs above $T_{ice}$ based on the Lagrangian model by using MIPAS measurements and ERA5 reanalysis data. Additionally, the observational

15 statistics presented can be utilized for comparison with chemistry-climate simulations.

# 1 Introduction

Polar stratospheric clouds (PSCs) form in winter and early spring in the polar stratosphere. Supercooled ternary solution (STS) droplets, nitric acid trihydrate (NAT), and ice particles are the three main types of PSCs. The surfaces of PSCs enable heterogeneous chemical reactions that convert reservoir species into chlorine radicals, subsequently leading to ozone depletion
20  in the polar winter stratosphere (Solomon et al., 1986; Solomon, 1999). Denitrification through the sedimentation of large NAT PSC particles also contributes to prolonged ozone depletion, as it reduces the concentration of $NO_2$ while increasing $Cl_2$. The formation processes and conditions are summarized in Lambert et al. (2012) and Tritscher et al. (2021), highlighting the pivotal role of temperature in these processes.

In the Antarctic, synoptic low temperatures typically occur in midwinter, causing temperatures to drop below the formation
25  thresholds and resulting in substantial formation of PSCs (Campbell and Sassen, 2008). However, temperature perturbations can also trigger the development of PSCs, even in cases where synoptic-scale temperatures are higher than the formation thresholds (Carslaw et al., 1998b; Rivière et al., 2000; Dörnbrack et al., 2020; Orr et al., 2020). PSCs triggered by small-scale temperature fluctuations have been observed predominantly in various mountain regions, including Greenland and Scandinavia in the Arctic, as well as the Antarctic Peninsula and the Transantarctic Mountains in the Antarctic. For example, over the
30  Antarctic Peninsula, the Cloud-Aerosol Lidar Infrared Pathfinder Satellite Observations (CALIPSO) detected 63 % of ice PSC volumes during gravity wave events over the 2006 – 2010 Antarctic winters (Noel and Pitts, 2012). The mountain waves were also verified by Höpfner et al. (2006) and Eckermann et al. (2009) as a trigger for the appearance of the Antarctic NAT belt, originating from ice particles over the Antarctic Peninsula in June 2003, as evidenced by measurements from the Michelson Interferometer for Passive Atmospheric Sounding (MIPAS). Analyses based on four years of CALIPSO data revealed that 75 %
35  of ice PSCs and 50 % of NAT mixtures in both hemispheres were closely linked to mountain wave activity (Alexander et al., 2013). The influence of gravity waves, which result in small-scale temperature fluctuations triggering the formation of PSCs, has been discussed in WMO (2018). Additionally, WMO (2022) has addressed that the occurrence of PSCs over the Antarctic Peninsula is linked to frequent mountain wave activities.

Trajectories simulated by Lagrangian models offer valuable insights into the formation and evolution of PSCs (Santee et al.,
40  2002; Lambert et al., 2012; Hoffmann et al., 2017b; Tritscher et al., 2019). Based on multiple Arctic vortex trajectories, Carslaw et al. (1999) has unveiled the significance of temperature perturbations induced by mountain waves in generating solid PSC particles in the east of Greenland, the Norwegian mountains, and the Urals during December 1994 and January 1995. Temperature perturbations identified along trajectories have emerged as a crucial factor influencing PSC formation (Lambert et al., 2016). However, the subgrid-scale temperature fluctuations related to gravity waves may not be fully resolved
45  or underestimated in global reanalyses or coarse-resolution chemistry-climate models.

In this study, our primary focus is to investigate the occurrence of ice PSCs observed by Envisat MIPAS (Spang et al., 2004, 2018) and characterized by temperatures above the ice existence threshold ($T_{ice}$), as derived from by ERA5 reanalysis (Hersbach et al., 2020). Ice PSCs are observed at temperature-based sampling points during the Arctic (November – February) and Antarctic (June – September) winters, covering the period from 2002 to 2012. Additionally, leveraging the capabilities of

50  the Massive-Parallel Trajectory Calculations (MPTRAC) model (Hoffmann et al., 2016, 2022) developed at the Jülich Super-
computing Centre, we explore the temperature variations along the backward trajectories driven by ERA5 data to comprehend
their impact on ice PSC occurrence.

The study begins with a comprehensive overview of the data and methodology, detailing the retrieval of ice PSCs from
MIPAS, introducing the MPTRAC model, and describing the detection of temperature fluctuations (Sect. 2). Spatio-temporal
55  features of ice PSCs are analyzed in Sect. 3.1, followed by an examination of ice PSC observations above $T_{ice}$ in Sect. 3.2.
The Lagrangian history and temperature fluctuations of ice PSCs above $T_{ice}$ are explored in Sect. 3.3 and 3.4, respectively. The
correlation between ice PSC occurrence above $T_{ice}$ and mountain waves is investigated in Sect. 3.5. Uncertainties inherent in
the study are discussed in Sect. 4, while the main conclusions drawn from the analysis are summarized in Sect. 5.

## 2  Data and method

### 2.1  MIPAS observations of PSCs

60

The Michelson Interferometer for Passive Atmospheric Sounding (MIPAS) onboard the Envisat satellite measured high-
resolution limb infrared spectra in the $4-15\,\mu$m wavelength range from the mid-troposphere to the mesosphere (Fischer et al.,
2008). The Envisat satellite, which was in a sun-synchronous low Earth orbit (98.4° inclination), was able to capture measure-
ments with coverage up to both poles, attributable to an extra poleward tilt of the primary mirror. From 2002 to 2004, MIPAS
65  collected samples with a resolution of $3\,$km (vertical) $\times\,30\,$km (horizontal) at the tangent point. Later, between January 2005
and April 2012 the vertical sampling below 21 km was optimized to 1.5 km in the nominal measurement mode. MIPAS ceased
operation on 8 April 2012 due to the sudden loss of contact with Envisat.

The cloud index (CI) (Spang et al., 2001) is known to be sensitive to PSCs (Spang et al., 2004). A fast prototype processor
for retrieving cloud parameters from MIPAS (MIPclouds) is described in Spang et al. (2012), where PSC detections and their
70  cloud top heights are obtained by a step-like data processing approach of up to five detection methods. More than 600,000
modeled MIPAS-like spectra are included to represent PSC composition (Spang et al., 2012). A Bayesian probabilistic scheme
identifies the different types of PSCs in MIPAS measurements based on the combination of CI, NAT-index (NI), and brightness
temperature differences (Spang et al., 2016). Eight classes (-1: unclassified (non-cloudy), 0: unknown, 1: ice, 2: NAT, 3: STS,
4: ICE_NAT, 5: STS_NAT, and 6: ICE_STS) are defined based on the normalized product probability for each spectrum (Spang
75  et al., 2016, 2018).

In this study, ice PSCs were extracted from the MIPAS/Envisat Observations of Polar Stratospheric Clouds dataset (Spang,
2020). Typically, the tangent point, which is the line of sight that penetrates the atmosphere down to a minimum altitude,
serves as the reference point for MIPAS observations of PSC locations (Fischer et al., 2008). However, this is not optimal for
cloud observations in the limb, where the precise location of the cloud along the line of sight remains uncertain. Depending
80  on the atmospheric conditions, the cloud's location could deviate by several hundred kilometers horizontally, either in front or
behind the tangent point. Therefore, instead of using the tangent point of the sample, we employ the point with the minimum
temperature difference ($\Delta T_{ice\_min}$) between the frost point temperature ($T_{ice}$) and the environmental temperature along the line

of sight, up to a maximum altitude of 30 km, to identify the most probable position of the ice PSC observation. Observations at $\Delta T_{\text{ice\_min}}$ help to identify the most favorable conditions for the ice PSCs. Here, $T_{\text{ice}}$ and the temperature along the line of sight were derived from ERA-Interim reanalysis for the identification of $\Delta T_{\text{ice\_min}}$ of the MIPAS observations.

In addition, only data with a CI > 1.2 (not completely optically thick) and CI < 4 (detection threshold) were used in this study. All detected ice PSCs met the conditions for potential vorticity ≥4, heights between 14 and 30 km, and only at altitudes up to −6.1 km below the cloud top. All of the above criteria helped to ensure that measurements are located in the stratosphere and that potentially optically thick cases were excluded. Northern hemispheric (NH) PSCs were based on data for the Arctic winter (December – February), and southern hemispheric (SH) PSCs were based on data for the Antarctic winter (June – September) at latitudes higher than 50° from December 2002 to February 2012. Data from 2002, 2004 in the Antarctic and 2003 in the Arctic were excluded due to many missing observations.

## 2.2 The MPTRAC model and the reanalyses

Lagrangian particle dispersion models can precisely represent atmospheric transport processes by computing air parcel trajectories. The Massive-Parallel Trajectory Calculations (MPTRAC) model (Hoffmann et al., 2016, 2022) was developed to study large-scale atmospheric transport in the free troposphere and stratosphere. The MPTRAC model includes a variety of modules and tools, i.e., modules of advection, turbulent diffusion, subgrid-scale wind fluctuations, convection, sedimentation, wet and dry deposition, hydroxyl chemistry, exponential decay, and boundary conditions. In the advection module, air parcel trajectories are calculated based on given wind fields from meteorological data sets. Following the FLEXPART model (Stohl et al., 2005), turbulent diffusion and subgrid-scale wind fluctuations are simulated by MPTRAC by adding stochastic perturbations to the trajectories. The MPTRAC model was applied to calculate trajectories for MIPAS PSC observations Hoffmann et al. (2017b) and the trajectories calculated from the MPTRAC model were evaluated by superpressure balloons for the polar lower stratosphere Hoffmann et al. (2017a). In this study, the advection module of MPTRAC is applied to calculate backward trajectories based on PSC observations. The tool for meteorological data sampling is used to obtain corresponding meteorological data for the MIPAS PSC observations, including the temperature, humidity, and frost point along the trajectories (Hoffmann et al., 2022).

The ERA-Interim reanalysis (Dee et al., 2011) was used only for identifying the location of ice PSCs ($\Delta T_{\text{ice\_min}}$) along the line of sight of MIPAS in this study. This reanalysis was conducted by the European Centre for Medium-Range Weather Forecasts (ECMWF) using the Integrated Forecast System (IFS) Cycle 31r2, released in December 2006. ERA-Interim provides 6-hourly data spanning from January 1979 to August 2019, with a horizontal resolution of approximately 79 km and 60 model levels from the surface up to 0.1 hPa.

Other analyses, i.e. the $T_{\text{ice}}$ and trajectory calculations in this study were based on the fifth-generation reanalysis (ERA5 Hersbach et al., 2020) from ECMWF. ERA5 provides hourly meteorological data with a horizontal resolution of about 31 km on 137 hybrid sigma/pressure levels vertically from the surface to 0.01 hPa. The evaluation of MPTRAC trajectory calculations was assessed by using different meteorological reanalyses (Hoffmann et al., 2017b; Rößler et al., 2018; Hoffmann et al., 2019).

4

By comparing the ERA5 and ERA-Interim reanalyses, the Lagrangian transport was found to be significantly impacted by the ERA5 data (Hoffmann et al., 2019).

## 2.3 Ice PSCs and detection of temperature fluctuations

In this study, we aim to conduct a statistical analysis of ice PSCs where the temperature at the MIPAS observation is above the frost point temperature ($T_{ice}$) derived from ERA5 reanalyses. $T_{ice}$ was calculated from pressure and $H_2O$ in ERA5 using the equation proposed by (Marti and Mauersberger, 1993), which is derived from direct measurements of the vapor pressure down to temperatures of 170 K. The ice frost point indicates the temperature threshold below which ice particles can exist.

Ice particles nucleate homogeneously at temperatures $3 - 4$ K below $T_{ice}$ (Koop et al.), and heterogeneously on solid hydrates at temperatures $0.1 - 1.3$ K below $T_{ice}$ (Carslaw et al., 1998a; Koop et al., 1998; Fortin et al., 2003; Engel et al., 2013; Voigt et al., 2018). Therefore, in addition to the temperature threshold of $T_{ice}$, we also considered temperature thresholds ($T_{ice}-3$ K and $T_{ice}-1.5$ K) in our statistical assessment of the PSC occurrence.

The variance of the temperature cooling rate over 6 hours was used to identify temperature fluctuations along the kinematic backward trajectory. We empirically identified potentially significant temperature fluctuations using a variance of the temperature cooling rate exceeding $0.9\,\mathrm{K\,h^{-2}}$ and a temperature less than 10 K above $T_{ice}$ as the selection criteria. It is important to note that the amplitudes of temperature fluctuations are often underestimated in the ERA5 reanalysis (Hoffmann et al., 2017b; Orr et al., 2020; Weimer et al., 2021). Therefore, small thresholds are needed to detect potentially relevant wave events for PSC occurrence.

## 3 Results

### 3.1 Ice PSCs detected by MIPAS

Instead of the tangent point, we used the point with the minimum temperature difference ($\Delta T_{ice\_min}$) between $T_{ice}$ and the environmental temperature $T$ along the line of sight up to a maximum altitude of 30 km to obtain the position of the ice PSC observation. The spatial and vertical distribution of the multi-year averaged occurrence frequency of ice PSCs from MIPAS is presented in Fig. 1. In the Antarctic, ice PSCs are observed at all latitudes south of 65°, but favor the longitude range ±90° with the highest occurrence frequency over 16 %. Over the seasons, ice PSCs are predominantly observed during midwinter, from late June to September, and are mostly detected at the altitude range of 22 km to 28 km. In the Arctic, ice PSCs are mainly observed within the longitude range of 60°W to 120°E with the highest occurrence frequency of about 2 %, which is a favored region for the locations of the Arctic vortex and wave activities (Alexander et al., 2009; Zhang et al., 2016). The highest occurrence frequencies of ice PSCs in the Arctic are found in February at an altitude range of 22 km to 26 km (Fig. 1d).

Figure 2 shows the averaged occurrence frequency of ice PSCs as a function of temperature difference to $T_{ice}$ during the period $2002 - 2012$. In both polar regions, ice PSCs observed at $\Delta T_{ice\_min}$ are predominantly found below the frost point temperature. However, ice PSCs in the Arctic have higher temperatures than those in the Antarctic. There are approximately
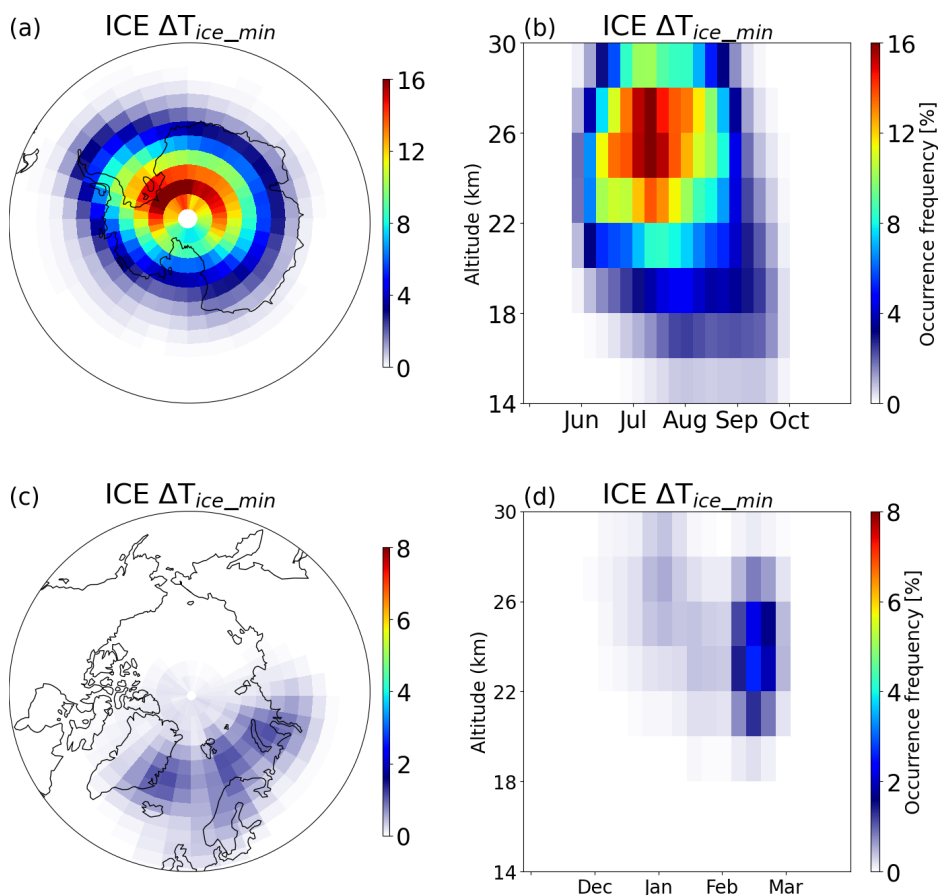
**Figure 1.** Occurrence frequency of ice PSCs (detected PSCs with respect to all measurements) at the point with the minimum temperature difference between $T_{ice}$ and $T$ along the line of sight ($\Delta T_{ice\_min}$) derived from MIPAS observations. The data is gridded on $3° \times 5°$ boxes and the time series are averaged over 7 days and 2 km height bins.

56 %, and 28 % of ice PSCs in the Arctic and Antarctic, respectively, detected at temperatures higher than the local frost point temperature ($T_{ice}$) derived from the ERA5 reanalysis. Since ice PSC particles nucleate at temperatures slightly lower than $T_{ice}$ (Voigt et al., 2005), we included the two temperature thresholds, denoted as $T_{ice} - 3\,\mathrm{K}$ for homogeneous nucleation and

150    $T_{ice} - 1.5\,\mathrm{K}$ for heterogeneous nucleation. Regarding nucleation temperatures, the frequency of ice PSCs exceeds 90 % when temperatures are above $T_{ice} - 1.5\,\mathrm{K}$ in both hemispheres and surpass 100 % when temperatures are above $T - T_{ice} - 3\,\mathrm{K}$). This implies that the majority of ice PSCs were above their nucleation temperature, based on the temperature and water vapor data from the ERA5 reanalysis.
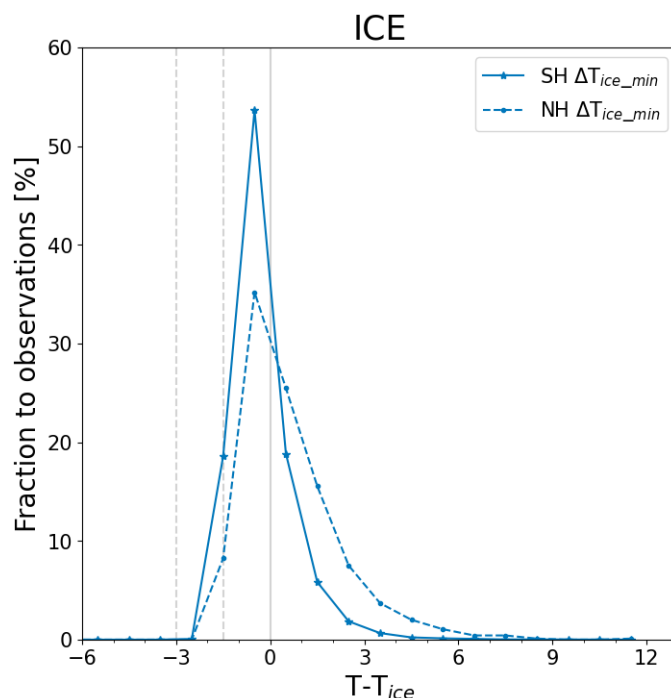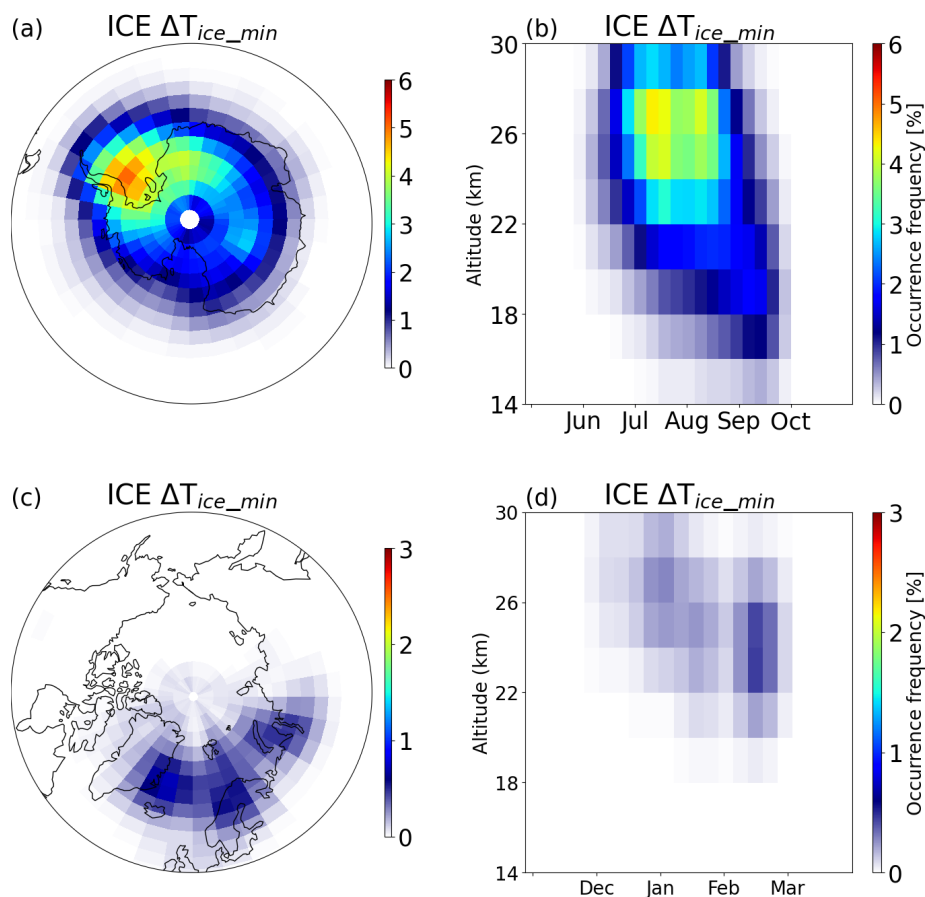
**Figure 2.** Occurrence frequency of ice PSCs as a function of the temperature difference $(T - T_{\text{ice}})$ with the bin size of 1 K. Solid lines represent data from the Antarctic, while dashed lines represent data from the Arctic. Two vertical gray dashed lines are included at $T - T_{\text{ice}}$ = $-3$ K and $T - T_{\text{ice}}$ = $-1.5$ K for reference.

### 3.2 Characteristics of ice PSC observations above $T_{\text{ice}}$

In the Antarctic, ice PSCs above $T_{\text{ice}}$ are predominantly concentrated around the Antarctic Peninsula and its downwind direction with a peak value of about 5 %, notably towards the Weddell Sea (see Fig. 3a). In the Arctic, the spatial distribution pattern of ice PSCs above $T_{\text{ice}}$ is similar to that of all the observed ice PSCs, which are distributed across areas such as East Greenland and Scandinavia with peak values of about 1 %, along with their respective downwind directions (see Fig. 3c). The vertical and temporal evolution of ice PSCs above $T_{\text{ice}}$ shows that they are mainly concentrated in deep winter, spanning from July to the middle of August in the Antarctic. Ice PSCs above $T_{\text{ice}}$ (Fig. 3b) demonstrate a descending trend in altitude as late winter approaches, particularly in August and September. A similar pattern is observed in the Arctic, where the vortex warms from above, leading to a downward shift in later winter (Rosenfield et al., 1994).

Figure 4 shows the fractions of ice PSCs above $T_{\text{ice}}$ with respect to all detected PSCs as a function of winter months and years. In the Antarctic (Fig. 4a,b), the fraction of ice PSCs above $T_{\text{ice}}$ increases from 15 % in June to 60 % in September, remaining relatively stable across the years. In the Arctic (Fig. 4c,d), the fraction of ice PSCs above $T_{\text{ice}}$ is comparable in January and February and relatively high in December due to less ice PSC observations. However, their fraction shows substantial variability from year to year. Notably, there is a lower occurrence of ice PSCs above $T_{\text{ice}}$ in the years 2005 and 2011, which is probably

**Figure 3.** Similar to Fig. 1, occurrence frequency of ice PSCs above $T_{ice}$ at $\Delta T_{ice\_min}$ only.

due to the few ice PSCs observed in those two years. The peak value observed in 2008 could be linked to the eruption of the Kasatochi volcano (Waythomas et al., 2010). The larger temperature variability and less stable polar vortex in the Arctic

170 (Newman et al., 2001) compared to the Antarctic cause larger variability in ice PSC occurrence in the Arctic than in the Antarctic. When considering the application of nucleation temperature thresholds ($T_{ice} - 3\,\mathrm{K}$ and $-1.5\,\mathrm{K}$), the fraction of ice PSCs above $T_{ice} - 3\,\mathrm{K}$ and $-1.5\,\mathrm{K}$ significantly increases. In both hemispheres, this fraction exceeds 95 %.
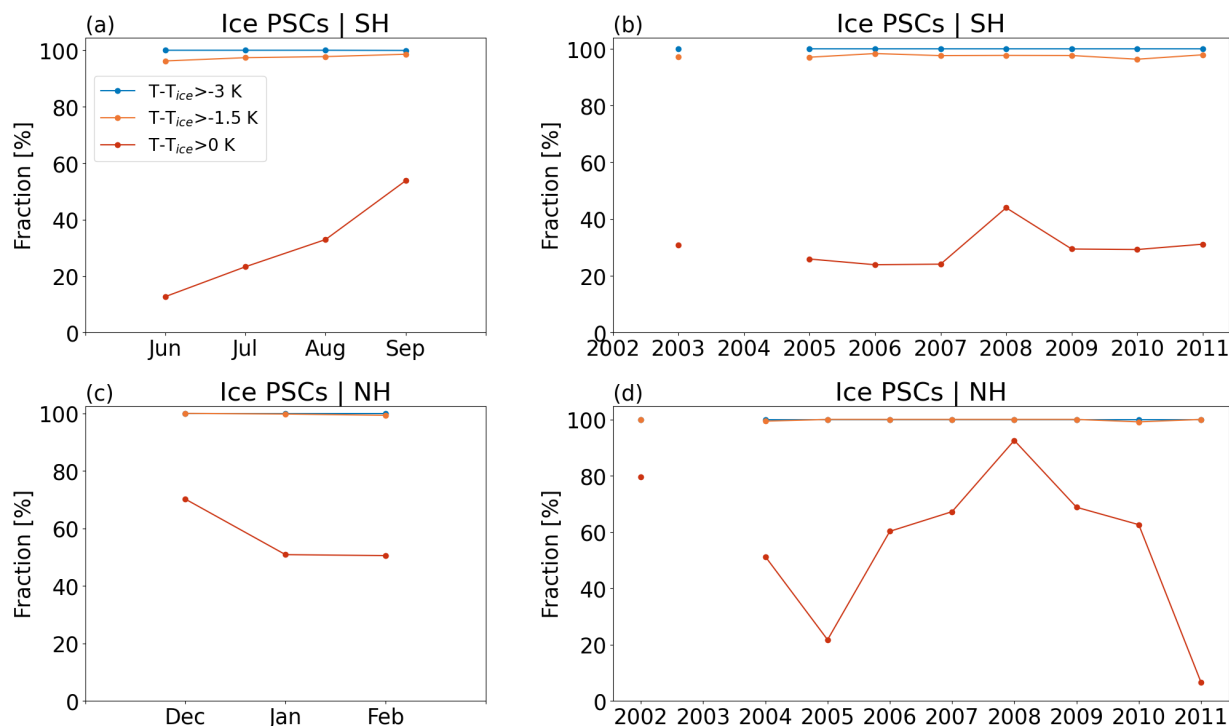
**Figure 4.** Fraction of ice PSCs above $T_{ice}$ to all detected PSCs across different months and years. Red lines represent the fractions with $T - T_{ice} > 0$ K, while orange and blue lines represent the fractions with $T - T_{ice} > -1.5$ K and $> -3$ K. The data for the Antarctic in 2002 and 2004, as well as for the Arctic in 2003, are missing due to missing MIPAS observations.

## 3.3 Temperature history of ice PSC observations above $T_{ice}$

To gain deeper insights into the history of the ice PSCs observations above $T_{ice}$, we employed the MPTRAC model to calculate

175    24-hour backward trajectories from the point of observation at $\Delta T_{ice\_min}$. Fig. 5 displays the fraction of ice PSCs above $T_{ice}$ along the backward trajectories, ranging from time ($t$) $t = -24$ (h) to $t = 0$. The most significant decrease of the fraction occurs within the 6 hours preceding the observations. During this period, the fractions of ice PSCs above $T_{ice}$ decrease by about 17 percentage points (pp) and 10 pp in the Arctic and Antarctic, respectively, from the observation point at $\Delta T_{ice\_min}$ to $t = -6$ h. A similar trend is observed for ice PSCs with the temperature threshold $T = T_{ice} - 1.5$ K, albeit with relatively smaller

180    fractions. It means that 6 h before the observation, temperatures of most ice PSCs (about 65 % in the Arctic and 85 % in the Antarctic) are below $T_{ice}$. Nevertheless, a portion of the ice PSCs (17 pp and 10 pp in the Arctic and Antarctic) experienced a temperature decrease below $T_{ice}$ from the MIPAS observation point to 6 hours preceding the observations.
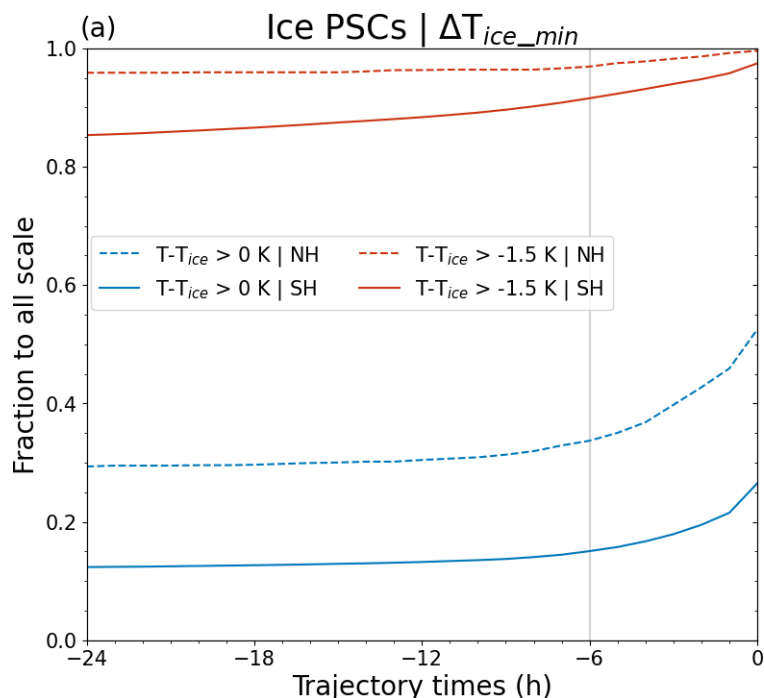
**Figure 5.** Fraction of ice PSCs above $T_{ice}$ within 24-hour backward trajectory with respect to all detected ice PSCs.

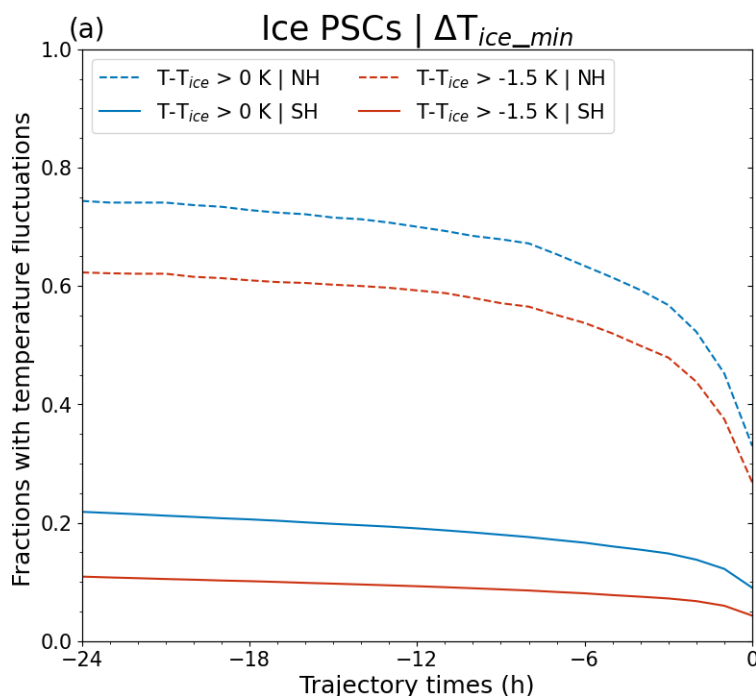## 3.4 Temperature fluctuations along the backward trajectories

Gravity waves are recognized as a key driver for the occurrence of ice PSCs above $T_{ice}$ in warmer environments. Monitoring
185 temperature fluctuations provides a valuable indicator for assessing the influence of gravity waves on PSC occurrence. Detecting these temperature fluctuations is therefore crucial for gaining insights into the history and evolution of ice PSCs above $T_{ice}$. In this study, ERA5 temperature data was used to assess the influence of temperature fluctuations on the occurrence of ice PSCs along the trajectories.

An example is presented in Fig. 6 to show how we detected temperature fluctuations along the backward trajectories. The
190 temperature cooling rate and its variance were calculated to identify the temperature fluctuations of the ice PSCs. In this example, temperature fluctuations were found over $t = -10$h to $t = -0$, when the temperature cooling rate variance exceeds $0.9\,\mathrm{K\,h^{-2}}$, and the temperature is no more than 10 K above $T_{ice}$. Those detected temperature fluctuations coincide with areas exhibiting high $4.3\,\mu\mathrm{m}$ brightness temperature (BT) variances as retrieved from NASA's Atmospheric Infrared Sounder (AIRS, Fig. 6b), indicating the presence of stratospheric gravity waves (Hoffmann et al., 2013, 2017b). In this particular example,
195 the ERA5 temperature fluctuation over the east coast of Greenland coincides with variations in AIRS brightness temperature, attributed to the influence of gravity waves. This correlation suggests a potential connection to the occurrence of ice PSCs.

The cumulative fraction of ice PSCs above $T_{ice}$ with temperature fluctuations relative to all ice PSCs above $T_{ice}$ is presented in Fig. 7. Generally, this cumulative fraction increases as we trace backward in time. At the observation points, the mean
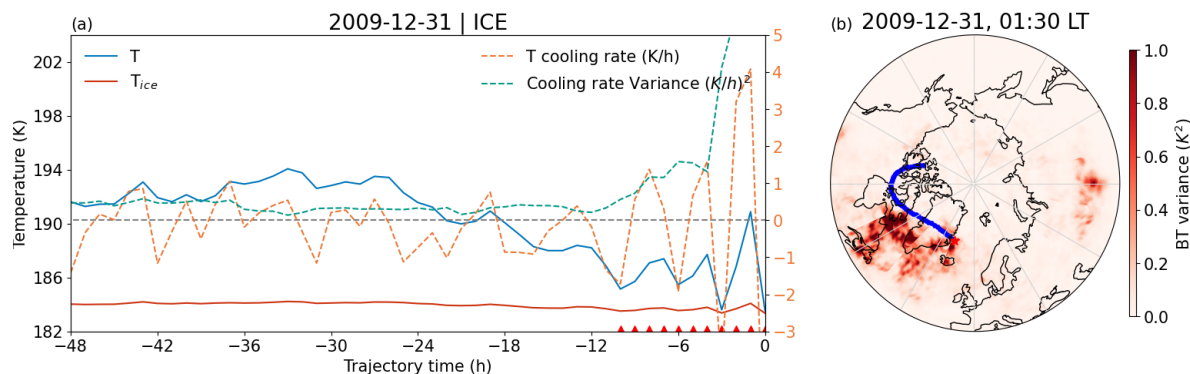
**Figure 6.** Example of detecting temperature fluctuations along backward trajectories. The example shows an ice PSC above $T_{ice}$ observed on December 31, 2009. a) The temperature ($T$) and $T_{ice}$ from ERA5 are shown as solid blue and orange lines, and the temperature cooling rate and its variance are dashed orange and green lines. Red triangles indicate the detected temperature fluctuations along the backward trajectory over $t = -10$h to $t = -0$. b) The brightness temperature (BT) variances detected by AIRS at local time 01:30 are shown as a contour surface in the map. The blue curve shows the backward trajectory of ice PSC and the red star in the map indicates the location of the observed ice PSC at $\Delta T_{ice\_min}$.



**Figure 7.** The cumulative fraction of ice PSCs above $T_{ice}$ with temperature fluctuations along the backward trajectory with respect to all ice PSCs above $T_{ice}$. Blue lines represent temperatures above $T_{ice}$, while red lines represent temperatures $> T_{ice} - 1.5$ K.

fractions of ice PSCs above $T_{ice}$ with temperature fluctuations are 33 % in the Arctic and 9 % in the Antarctic. As we progress

200    to $t = -24\,h$ (24 hours before the MIPAS observation), approximately 74 % of ice PSCs above $T_{ice}$ in the Arctic, and about

22 % in the Antarctic, could be related to temperature fluctuations (see Table 1). This suggests that the temperature fluctuations

as resolved in ERA5 play a significant role in the presence of ice PSCs above $T_{ice}$, particularly in the Arctic.

Figure 8 presents the spatial distribution of ice PSCs above $T_{ice}$ with temperature fluctuations at the observation point.

The patterns closely resemble the occurrence frequency of ice PSCs above $T_{ice}$. In the Antarctic, ice PSCs above $T_{ice}$ with

205    temperature fluctuations are primarily concentrated at and around the Antarctic Peninsula and the Weddell Sea. Notably, two

prominent hotspots of ice PSCs above $T_{ice}$ with temperature fluctuations are situated downwind of the Antarctic Peninsula

and Victoria Land. In the Arctic, ice PSCs above $T_{ice}$ with temperature fluctuations are observed within the longitude range

of 60°W to 120°E, encompassing the east coast of Greenland and Northern Scandinavia. In summary, the presence of ice

PSCs above $T_{ice}$ with temperature fluctuations is associated with mountain regions and their downwind areas. This observation

210    strongly suggests a correlation with orographic waves with ice PSCs above $T_{ice}$.
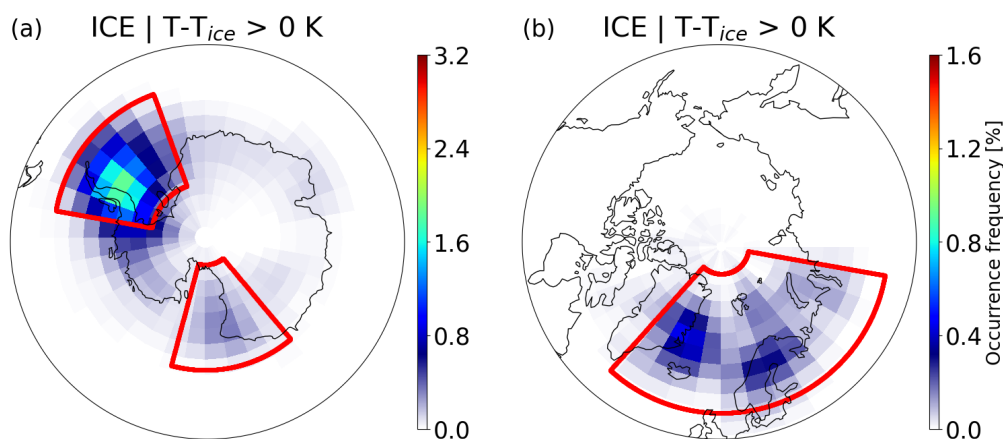


**Figure 8.** Occurrence frequency of ice PSCs above $T_{ice}$ with temperature fluctuations at the observation point relative to all measurements in the Antarctic and the Arctic, respectively. Three specific mountain regions, the Antarctic Peninsula (AP), the Transantarctic Mountains (TM), and the mountain region in the Northern Hemisphere (NH-M), are marked with red boxes.

### 3.5   Correlation between mountain waves and ice PSCs above $T_{ice}$

To further explore the potential correlation of orographic waves and the occurrence of ice PSCs above $T_{ice}$, we selected two

mountain regions in the Antarctic and one in the Arctic (indicated by red boxes in Fig. 8). The defined mountain regions are

the Antarctic Peninsula (AP: [58° – 83°S, 35° – 80°W]), the Transantarctic Mountains (TM: [62° – 85°S, 165°W – 150°E])

215    and mountain regions in the Northern Hemisphere (NH-M: [55° – 85°N, 45°W – 90°E]). To quantify the potential influence of

mountain waves on the occurrence of ice PSCs above $T_{ice}$, we present the fractions of ice PSCs above $T_{ice}$ over these specified

mountain regions in Table 1, columns 3 – 5.

The fractions of ice PSCs above $T_{ice}$ related to mountain waves decrease as it gets closer to the observation point. At t=$-24$, the cumulative fraction of ice PSCs above $T_{ice}$ related to mountain waves are 9.4 % over the AP and 3.2 % over the TM. However, at the observation point ($t =0$), these fractions are considerably smaller. The fractions in the Arctic mountain regions are notably higher than those in the Antarctic, reaching 59 % at $t = -24$. This difference can be attributed to the more frequent occurrence of gravity wave activity in the Northern Hemisphere, although the size of the selected area also influences the results. In conclusion, ice PSCs above $T_{ice}$ in the Arctic are more susceptible to the effects of mountain waves.

**Table 1.** Cumulative fraction of ice PSCs above $T_{ice}$ related to mountain waves at different backward trajectory times relative to all ice PSCs above $T_{ice}$. Mountain regions are the Antarctic Peninsula (AP), the Transantarctic Mountains (TM) and mountain regions in the Northern Hemisphere (NH-M)

| Time | Ice PSCs at $\Delta T_{ice\_min}$ | | | | |
| --- | --- | --- | --- | --- | --- |
| | SH | NH | AP | TM | NH-M |
| t= 0 | 9.0% | 33.0% | 4.3% | 0.9% | 27.0% |
| t=$-6$ | 16.6% | 63.4% | 7.6% | 1.6% | 50.3% |
| t=$-12$ | 19.0% | 70.0% | 8.5% | 2.0% | 55.9% |
| t=$-18$ | 20.6% | 72.8% | 9.0% | 2.6% | 57.6% |
| t=$-24$ | 21.8% | 74.4% | 9.4% | 3.2% | 58.7% |

## 4 Discussion

### 4.1 PSC detections at warm environment

In this study, we analyzed the MIPAS-observed ice PSCs. We found that in the Arctic approximately 56 %, and in the Antarctic 28 % of the observed ice PSCs are detected at temperatures above $T_{ice}$ derived from ERA5 reanalysis. The occurrence of ice PSCs on warm large spatial scales has already been reported in previous studies. For instance, Pitts et al. (2018, Fig. 12) present about 30 % of ice PSCs observed above the $T_{ice}$ in the Arctic and Antarctic based on CALIPSO measurements and about 20 % of ice PSCs ((Spang et al., 2018, Fig. 3)) are observed above $T_{ice}$ in the Antarctic from MIPAS observations at the tangent point over 2006 to 2012. Additionally, ice PSCs from MIPAS observations are reported in warm environments with temperatures around or warmer than $T_{NAT}$, i. e., 5 K or more above $T_{ice}$, based on ERA-Interim reanalysis (Hoffmann et al., 2017b, Fig.11). Even if ice PSCs are found in synoptic-scale warm environments, it is crucial to note that small-scale temperature fluctuations associated with orographic and gravity waves significantly influence the occurrence of ice PSCs (Dörnbrack et al., 2002; Alexander et al., 2013; Hoffmann et al., 2017b). While global reanalyses or coarse-resolution chemistry-climate models may not fully resolve subgrid-scale temperature fluctuations associated with gravity waves, ERA5 exhibits improved spatiotemporal resolution compared to ERA-Interim. However, it still tends to underestimate temperature fluctuations. The analysis applied in this study provides important information on the frequency and significance of these discrepancies.

## 4.2 Sampling uncertainty in MIPAS for ice PSC detection

240 To account for the uncertainty in cloud location within MIPAS observations, we have proposed a new reference point as an alternative to the tangent point. This reference point is defined as the location with minimum temperature difference ($\Delta T_{ice\_min}$) between the frost point temperature ($T_{ice}$) and the environmental temperature along the line of sight. Compared to ice PSCs detected at the tangent point shown in Figure 9, the altitudes of ice PSCs at $\Delta T_{ice\_min}$ (Fig. 1) are consistently higher, and the highest occurrence frequency of ice PSCs is approximately 4 km higher in the Antarctic at $\Delta T_{ice\_min}$ than at the tangent point,

245 and around 2 km higher in the Arctic. When comparing ice PSC observations derived from CALIOP (Pitts et al., 2018, Fig. 16 c), ice PSCs derived from MIPAS are relatively higher at the $\Delta T_{ice\_min}$. This discrepancy may be attributed to the large vertical field of view and coarse vertical sampling resolution of MIPAS. Consequently, cloud top heights of optically thick clouds in MIPAS are probably overestimated, on average by 0.75 km (Sembhi et al., 2012; Griessbach et al., 2020). Conversely, cloud top heights of optically thin PSCs observed at the tangent point are, on average, underestimated by 0 – 2 km and may reach up

250 to 8 km compared to CALIOP (Höpfner et al., 2009).
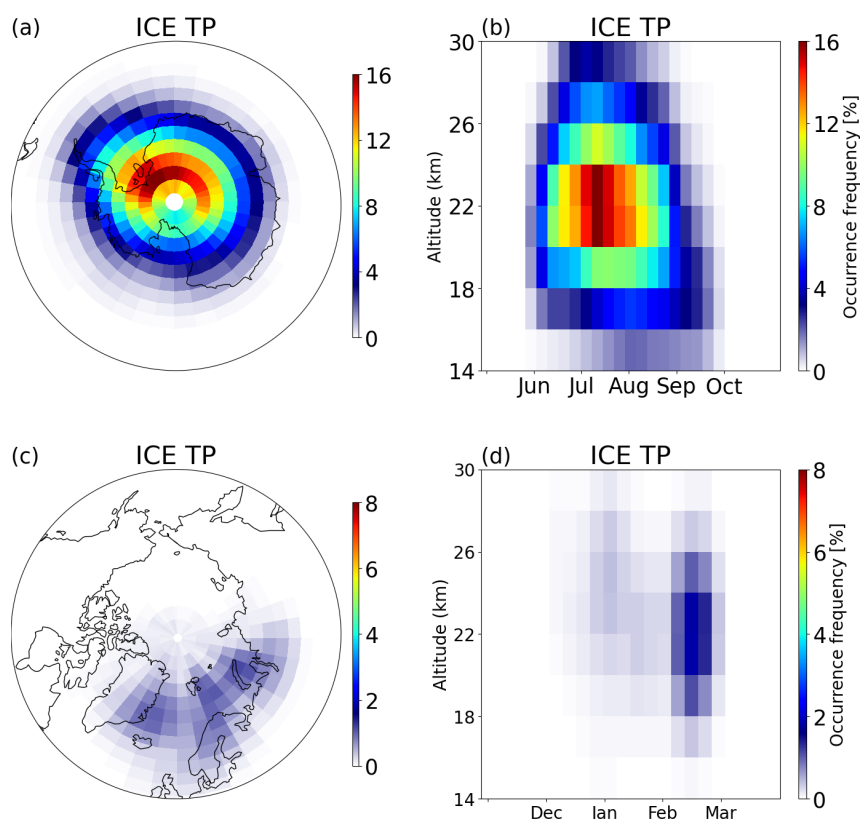


**Figure 9.** Occurrence frequency of ice PSCs (detected PSCs with respect to all measurements) at the tangent point from MIPAS observations. The data grid on the map is with a size of $3° \times 5°$ and time series are averaged over 7 days. It compares with Fig. 1, showing the same statistics for $\Delta T_{ice\_min}$.

Furthermore, when considering ice PSC observations as a function of $T - T_{\text{ice}}$, we observe that more ice PSCs are located above $T_{\text{ice}}$ at the tangent point (red lines in Fig. 10) than at $\Delta T_{\text{ice\_min}}$ (gray lines) in both polar regions. The distribution of ice PSCs as a function of $T - T_{\text{ice}}$ is more comparable to the CALIOP observations (Pitts et al., 2018, Fig. 12) and (Tritscher et al., 2021, Fig. 14 a and c)) than that at the tangent point. Despite the height discrepancy, the location of $\Delta T_{\text{ice\_min}}$ is more

255 reasonable for the existence of ice PSCs, as MIPAS is more sensitive to optically thin PSCs than CALIOP (Sembhi et al., 2012; Griessbach et al., 2020). The method to detect PSC locations in MIPAS observations, based on $\Delta T_{\text{ice\_min}}$, complements the conventional tangent point approach and aids in determining cloud positions within this study.
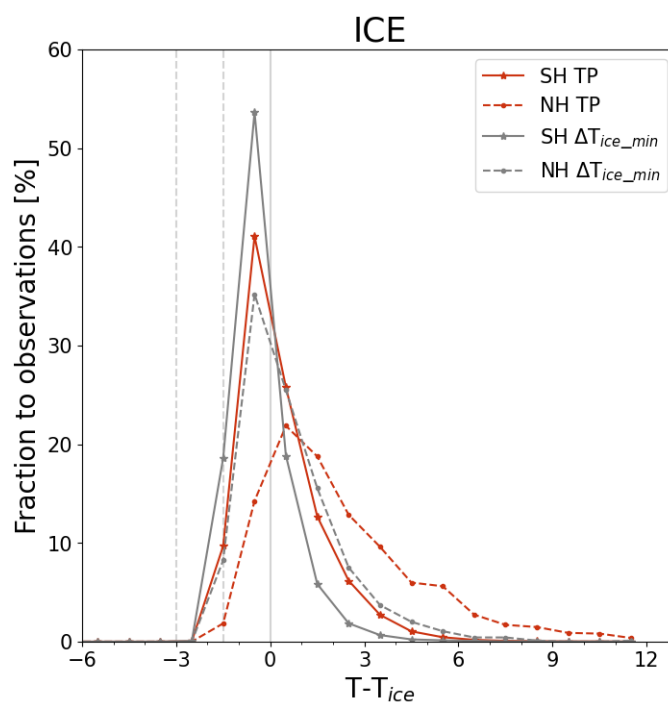


**Figure 10.** Occurrence frequency of ice PSCs detected at the tangent point (red lines) as a function of the temperature difference ($T - T_{\text{ice}}$).

### 4.3 Temperature and $\mathbf{T}_{ice}$ uncertainties in the ERA5 reanalysis

In this study, ambient temperatures of MIPAS observation points are interpolated from the ERA5 reanalysis, which offers

260 significantly improved spatial and temporal resolution compared to ERA-Interim (Hoffmann et al., 2019; Hersbach et al., 2020). Nevertheless, it is essential to acknowledge that the ERA5 reanalysis provides a global mean temperature estimate with an uncertainty of approximately 0.2 K compared to radiosonde measurements in the low and middle stratosphere (Simmons et al., 2020). Additionally, it is crucial to note that the ERA5 reanalysis may not fully resolve temperature perturbations associated with various factors such as convective updrafts, gravity waves, and other meso- to synoptic-scale features, as discussed in

265 Hoffmann et al. (2019). In particular, wave amplitudes are often underestimated. Consequently, there is a possibility that some temperature fluctuations are not resolved in ERA5 as discussed in Sect. 3.4.

In addition to ambient temperature, the calculation of $T_{ice}$ utilizes water vapor data ($H_2O$) from ERA5 and pressure, applying the equation proposed by Marti and Mauersberger (1993). However, the uncertainties in water vapor data from ERA5 remain unclear. Different methods for calculating $T_{ice}$ may introduce additional uncertainty in identifying ice PSCs above $T_{ice}$.

270 Figure 11 presents a sensitivity analysis of how $T_{ice}$ varies with water vapor content and pressure depending on the calculation method. Taking the example of a pressure level equal to 50 hPa (about 20 km of height), the $T_{ice}$ uncertainty is less than 2 K when the water vapor content ranges between typical stratospheric values of 2 ppm and 5 ppm. Different calculation methods for $T_{ice}$ result in negligible uncertainty, even though $T_{ice}$ calculated by Marti and Mauersberger (1993) is slightly warmer than following more recent methods (Murphy and Koop, 2005; WMO, 2008).
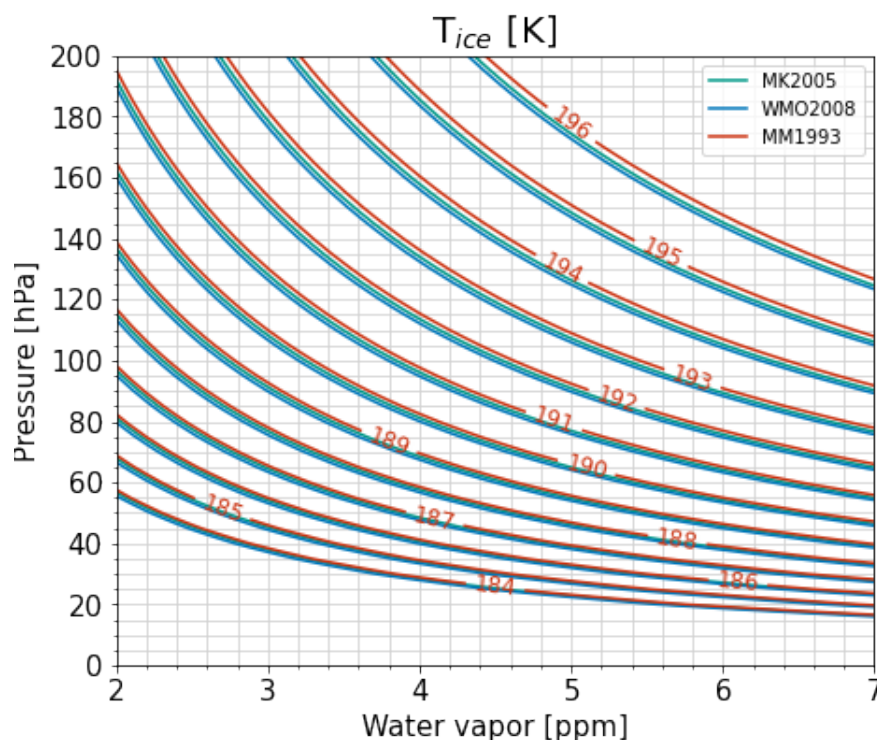


**Figure 11.** $T_{ice}$ uncertainty for different water vapor content and various calculation methods. MM1993, MK2005 and WMO2008 are methods proposed by Marti and Mauersberger (1993), Murphy and Koop (2005) and WMO (2008), respectively.

275 **4.4 Temperature fluctuation uncertainty**

The uncertainty in the selection of the threshold for the variance of the temperature cooling rate to detect temperature fluctuation events is illustrated in Fig. 12, where different thresholds for temperature cooling rate variance ($T_{crv}$) are examined, ranging from $0.6\,\mathrm{K\,h^{-2}}$ to $1.2\,\mathrm{K\,h^{-2}}$ in increments of $0.1\,\mathrm{K\,h^{-2}}$. As $T_{crv}$ increases, fewer temperature fluctuations are detected. For

instance, the highest fraction of ice PSCs above $T_{ice}$ with temperature fluctuations is observed at $T_{crv} = 0.6\,\mathrm{K\,h^{-2}}$, where the

280    fraction is approximately $30\,\%$ at $t = -24$. Conversely, the smallest fraction is found at $T_{crv} = 1.2\,\mathrm{K\,h^{-2}}$, with a fraction of $18\,\%$ at $t = -24$. However, the uncertainty in the choice of $T_{crv}$ decreases as the time approaches the observation point. At the MIPAS observation point, the uncertainty of $T_{crv}$ is within $1\,\mathrm{pp}$ in the Antarctic and $2\,\mathrm{pp}$ in the Arctic, with increments of $0.1\,\mathrm{K\,h^{-2}}$.
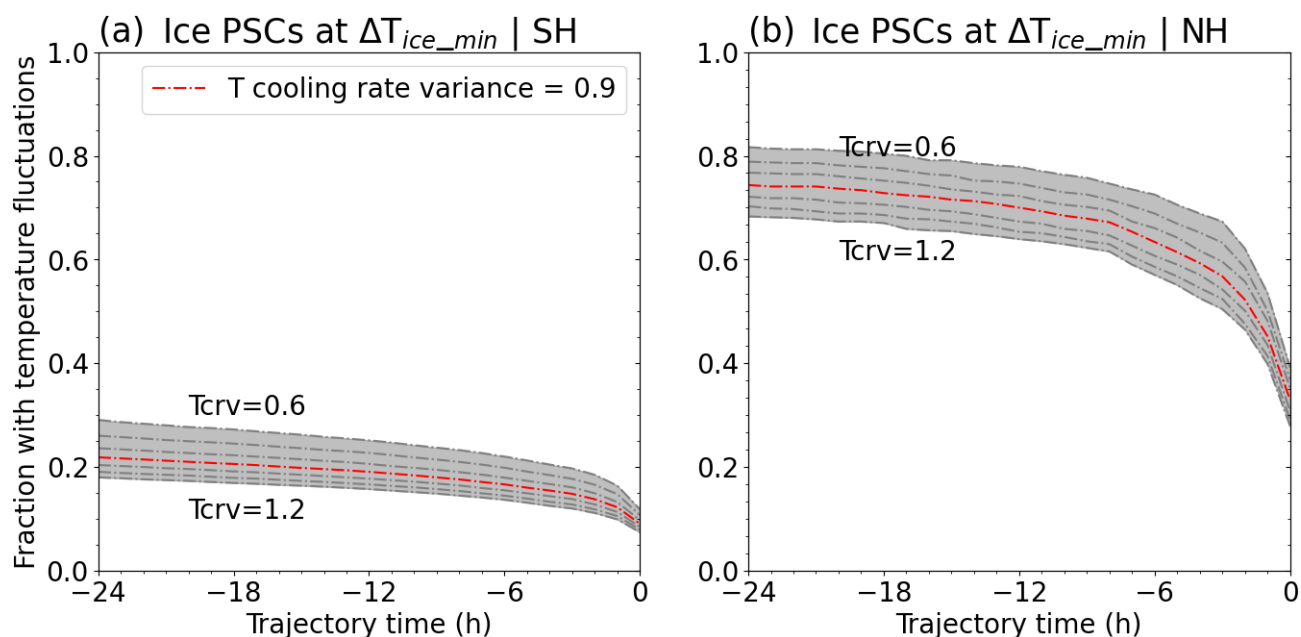


**Figure 12.** Cumulative fraction of ice PSCs above $T_{ice}$ with different temperature cooling rate variance thresholds ($T_{crv}$) for temperature fluctuation detection. $T_{crv} = 0.9, ..., 1.2\,\mathrm{K\,h^{-2}}$, the red dashed line is $T_{crv} = 0.9\,\mathrm{K\,h^{-2}}$ as selected for the statistical assessment.

The fractions of all ice PSCs above $T_{ice}$ passing through the defined mountain regions along the backward trajectory are

285    summarized in Table 2. These values exhibit a substantial increase compared to the fractions of ice PSCs above $T_{ice}$ with temperature fluctuations in mountain regions (Table 1). For example, at the MIPAS observation point in the AP region, the fraction of ice PSCs above $T_{ice}$ is $18.2\,\%$, whereas the fraction with temperature fluctuations is only $4.3\,\%$ as shown in Table 1. Comparing the values in Table 1 and Table 2, we find that although the majority of ice PSCs above $T_{ice}$ pass through specified mountain regions, only a limited number of them exhibit temperature fluctuations (Table 1). One possible reason for this

290    discrepancy is that the temperature fluctuations detected in our study may be underestimated due to the selected $T_{crv}$ threshold. Once again, unresolved temperature fluctuations in ERA5 reanalysis may contribute to these differences.

**Table 2.** Fraction of ice PSCs above $T_{ice}$ passing through specified mountain regions at different backward trajectory times.

| Time | Ice PSCs at $\Delta T_{ice\_min}$ | | |
|---|---|---|---|
| | AP | TM | NH-M |
| t= 0 | 18.2% | 8.2% | 73.9% |
| t=−6 | 20.7% | 11.7% | 79.6% |
| t=−12 | 22.6% | 16.4% | 83.7% |
| t=−18 | 24.0% | 22.7% | 83.9% |
| t=−24 | 25.3% | 30.0% | 84.1% |

## 5 Conclusions

This study examines a decade-long (2002 – 2012) record of ice PSCs derived from MIPAS/Envisat measurements. The points with the smallest temperature difference ($\Delta T_{ice\_min}$) between the frost point temperature ($T_{ice}$) and the environmental temperature along the line of sight, are proposed to provide the better location of ice PSC observation from MIPAS. The temperature at the ice PSC observations is analyzed based on the ERA5 reanalysis. Following this, we investigated the temperature history of the ice PSCs detected above $T_{ice}$ at the observation points along 24-hour backward trajectories.

In the MIPAS observations, ice PSCs are mostly observed in the longitude range of $\pm 90°$ in the Antarctic with peak values over 16 %, and between 60°W to 120°E in the Arctic during midwinter with peak values of about 2 %. Ice PSCs at $\Delta T_{ice\_min}$ are mostly detected in the altitude range of 22 km to 26 km, which is about 2 – 4 km higher above the tangent point.

The occurrence frequencies of ice PSCs as a function of temperature difference to $T_{ice}$ during the period 2002 – 2012 show that approximately 56 % and 28 % of the ice PSCs in the Arctic and Antarctic, respectively, are detected at temperatures higher than the local $T_{ice}$ based on the temperature and water vapor data from the ERA5 reanalysis. In the Antarctic, ice PSCs above $T_{ice}$ are predominantly located around the Antarctic Peninsula and its downwind direction, notably towards the Weddell Sea. In the Arctic, ice PSCs above $T_{ice}$ are distributed across mountain areas such as East Greenland and northern Scandinavia, along with their respective downwind directions. The ice PSCs above $T_{ice}$ are mainly concentrated in deep winter and demonstrate a descending trend in altitude as late winter approaches.

24-hour backward trajectories of the ice PSCs above $T_{ice}$ are calculated by using the MPTRAC model from the point of observation at $\Delta T_{ice\_min}$. The most significant change of the fraction of ice PSCs above $T_{ice}$ occurs within the 6 hours preceding the observations, in which 17 pp and 10 pp of ice PSCs in the Arctic and Antarctic experienced a temperature decrease below $T_{ice}$.

Furthermore, temperature fluctuations in backward trajectories were identified by the temperature cooling rate and its variance. At the observation point, the mean fractions of ice PSCs above $T_{ice}$ with temperature fluctuations are 33 % in the Arctic and 9 % in the Antarctic. 24 hours before the MIPAS observation the fraction of ice PSCs that have experienced temperature fluctuations increased to approximately 74 % in the Arctic and about 22 % in the Antarctic. Despite being underestimated in their magnitude, the temperature fluctuations in ERA5 have a significant correlation with the presence of ice PSCs above $T_{ice}$,

particularly in the Arctic. The ice PSCs above $T_{\text{ice}}$ with temperature fluctuations at the observation point are primarily concentrated in and around the Antarctic Peninsula and the Weddell Sea in the Antarctic and encompass the east coast of Greenland and Northern Scandinavia in the Arctic. This observation strongly suggests a correlation with orographic waves with ice PSCs above $T_{\text{ice}}$.

Across specified mountain regions, the fractions of ice PSCs above $T_{\text{ice}}$ related to mountain waves are 9.4 % over the AP and 3.2 % over the TM for observations at $\Delta T_{\text{ice\_min}}$ at $t = -24$. However, at the observation point ($t = -0$), these fractions are considerably smaller. The fractions in the Arctic mountain regions, reaching 59 %, are notably higher than those in the Antarctic. This difference can be attributed to the larger role of gravity wave activity in the occurrence of PSCs in the Northern Hemisphere and also to its larger selected region.

Our results are subject to several uncertainties. The uncertainties of temperature and water vapor in ERA5 data impact the identification of ice PSCs. We may also miss or underestimate many small-scale temperature fluctuations along the backward trajectories, which are not fully resolved in the ERA5 data, and the choice of the temperature cooling rate variance threshold for detecting gravity wave events has an impact on the results. Furthermore, substantial differences in cloud heights exist between MIPAS observations assigned to $\Delta T_{\text{ice\_min}}$ or assigned to the tangent point. Also, MIPAS measurements are integrated along the long limb path, but temperatures retrieved from ERA5 are for a spatial resolution of 31 km ($\Delta T_{\text{ice\_min}}$ or tangent point), which produces an uncertainty for identifying the distribution of ice PSCs relative to $T_{\text{ice}}$. Investigating the source of the discrepancies between ice PSC observations and warm temperatures is pertinent for understanding the formation of ice PSCs, as they require even lower temperatures.

# References

Alexander, S. P., Klekociuk, A. R., and Tsuda, T.: Gravity wave and orographic wave activity observed around the Antarctic and Arctic stratospheric vortices by the COSMIC GPS-RO satellite constellation, Journal of Geophysical Research: Atmospheres, 114, D17 103, https://doi.org/10.1029/2009JD011851, 2009.

350 Alexander, S. P., Klekociuk, A. R., McDonald, A. J., and Pitts, M. C.: Quantifying the role of orographic gravity waves on polar stratospheric cloud occurrence in the Antarctic and the Arctic, Journal of Geophysical Research: Atmospheres, 118, 11,493–11,507, https://doi.org/10.1002/2013JD020122, 2013.

Campbell, J. R. and Sassen, K.: Polar stratospheric clouds at the South Pole from 5 years of continuous lidar data: Macrophysical, optical, and thermodynamic properties, Journal of Geophysical Research: Atmospheres, 113, D20 204, https://doi.org/10.1029/2007JD009680, 355 2008.

Carslaw, K. S., Wirth, M., Tsias, A., Luo, B. P., Dörnbrack, A., Leutbecher, M., Volkert, H., Renger, W., Bacmeister, J. T., and Peter, T.: Particle microphysics and chemistry in remotely observed mountain polar stratospheric clouds, Journal of Geophysical Research: Atmospheres, 103, 5785–5796, https://doi.org/10.1029/97JD03626, 1998a.

Carslaw, K. S., Wirth, M., Tsias, A., Luo, B. P., Dörnbrack, A., Leutbecher, M., Volkert, H., Renger, W., Bacmeister, J. T., 360 Reimer, E., and Peter, T.: Increased Stratospheric Ozone Depletion Due to Mountain-Induced Atmospheric Waves, 391, 675–678, https://doi.org/10.1038/35589, 1998b.

Carslaw, K. S., Peter, T., Bacmeister, J. T., and Eckermann, S. D.: Widespread solid particle formation by mountain waves in the Arctic stratosphere, Journal of Geophysical Research: Atmospheres, 104, 1827–1836, https://doi.org/10.1029/1998JD100033, 1999.

Dee, D. P., Uppala, S. M., Simmons, A. J., Berrisford, P., Poli, P., Kobayashi, S., Andrae, U., Balmaseda, M. A., Balsamo, G., Bauer, 365 P., Bechtold, P., Beljaars, A. C. M., van de Berg, L., Bidlot, J., Bormann, N., Delsol, C., Dragani, R., Fuentes, M., Geer, A. J., Haimberger, L., Healy, S. B., Hersbach, H., Hólm, E. V., Isaksen, L., Kållberg, P., Köhler, M., Matricardi, M., McNally, A. P., Monge-Sanz, B. M., Morcrette, J.-J., Park, B.-K., Peubey, C., de Rosnay, P., Tavolato, C., Thépaut, J.-N., and Vitart, F.: The ERA-Interim reanalysis: configuration and performance of the data assimilation system, Quarterly Journal of the Royal Meteorological Society, 137, 553–597, https://doi.org/10.1002/qj.828, 2011.

370 Dörnbrack, A., Birner, T., Fix, A., Flentje, H., Meister, A., Schmid, H., Browell, E. V., and Mahoney, M. J.: Evidence for inertia gravity waves forming polar stratospheric clouds over Scandinavia, Journal of Geophysical Research: Atmospheres, 107, SOL 30–1–SOL 30–18, https://doi.org/10.1029/2001JD000452, 2002.

Dörnbrack, A., Kaifler, B., Kaifler, N., Rapp, M., Wildmann, N., Garhammer, M., Ohlmann, K., Payne, J. M., Sandercock, M., and Austin, E. J.: Unusual appearance of mother-of-pearl clouds above El Calafate, Argentina (50°21′S, 72°16′W), Weather, 75, 378–388, 375 https://doi.org/10.1002/wea.3863, 2020.

Eckermann, S. D., Hoffmann, L., Höpfner, M., Wu, D. L., and Alexander, M. J.: Antarctic NAT PSC belt of June 2003: Observational validation of the mountain wave seeding hypothesis, Geophysical Research Letters, 36, L02 807, https://doi.org/10.1029/2008GL036629, 2009.

Engel, I., Luo, B. P., Pitts, M. C., Poole, L. R., Hoyle, C. R., Grooß, J.-U., Dörnbrack, A., and Peter, T.: Heterogeneous formation of 380 polar stratospheric clouds – Part 2: Nucleation of ice on synoptic scales, Atmospheric Chemistry and Physics, 13, 10 769–10 785, https://doi.org/10.5194/acp-13-10769-2013, 2013.

Fischer, H., Birk, M., Blom, C., Carli, B., Carlotti, M., Von Clarmann, T., Delbouille, L., Dudhia, A., Ehhalt, D., Endemann, M., Flaud, J. M., Gessner, R., Kleinert, A., Koopman, R., Langen, J., López-Puertas, M., Mosner, P., Nett, H., Oelhaf, H., Perron, G., Remedios, J., Ridolfi, M., Stiller, G., and Zander, R.: MIPAS: An instrument for atmospheric and climate research, Atmospheric Chemistry and Physics,
385    8, 2151–2188, https://doi.org/10.5194/acp-8-2151-2008, 2008.

Fortin, T. J., Drdla, K., Iraci, L. T., and Tolbert, M. A.: Ice condensation on sulfuric acid tetrahydrate: Implications for polar stratospheric ice clouds, Atmospheric Chemistry and Physics, 3, 987–997, https://doi.org/10.5194/acp-3-987-2003, 2003.

Griessbach, S., Hoffmann, L., Spang, R., Achtert, P., von Hobe, M., Mateshvili, N., Müller, R., Riese, M., Rolf, C., Seifert, P., and Vernier, J.-P.: Aerosol and cloud top height information of Envisat MIPAS measurements, Atmospheric Measurement Techniques, 13, 1243–1271,
390    https://doi.org/10.5194/amt-13-1243-2020, 2020.

Hersbach, H., Bell, B., Berrisford, P., Hirahara, S., Horányi, A., Muñoz-Sabater, J., Nicolas, J., Peubey, C., Radu, R., Schepers, D., Simmons, A., Soci, C., Abdalla, S., Abellan, X., Balsamo, G., Bechtold, P., Biavati, G., Bidlot, J., Bonavita, M., De Chiara, G., Dahlgren, P., Dee, D., Diamantakis, M., Dragani, R., Flemming, J., Forbes, R., Fuentes, M., Geer, A., Haimberger, L., Healy, S., Hogan, R. J., Hólm, E., Janisková, M., Keeley, S., Laloyaux, P., Lopez, P., Lupu, C., Radnoti, G., de Rosnay, P., Rozum, I., Vamborg, F., Villaume, S., and Thépaut, J.-N.: The ERA5 global reanalysis, Quarterly Journal of the Royal Meteorological Society, 146, 1999–2049,
395    https://doi.org/10.1002/qj.3803, 2020.

Hoffmann, L., Xue, X., and Alexander, M. J.: A global view of stratospheric gravity wave hotspots located with Atmospheric Infrared Sounder observations, Journal of Geophysical Research: Atmospheres, 118, 416–434, https://doi.org/10.1029/2012JD018658, 2013.

Hoffmann, L., Rößler, T., Griessbach, S., Heng, Y., and Stein, O.: Lagrangian transport simulations of volcanic sulfur dioxide emissions: Impact of meteorological data products, Journal of Geophysical Research: Atmospheres, 121, 4651–4673,
400    https://doi.org/10.1002/2015JD023749, 2016.

Hoffmann, L., Hertzog, A., Rößler, T., Stein, O., and Wu, X.: Intercomparison of meteorological analyses and trajectories in the Antarctic lower stratosphere with Concordiasi superpressure balloon observations, Atmospheric Chemistry and Physics, 17, 8045–8061, https://doi.org/10.5194/acp-17-8045-2017, 2017a.

405 Hoffmann, L., Spang, R., Orr, A., Alexander, M. J., Holt, L. A., and Stein, O.: A decadal satellite record of gravity wave activity in the lower stratosphere to study polar stratospheric cloud formation, Atmospheric Chemistry and Physics, 17, 2901–2920, https://doi.org/10.5194/acp-17-2901-2017, 2017b.

Hoffmann, L., Günther, G., Li, D., Stein, O., Wu, X., Griessbach, S., Heng, Y., Konopka, P., Müller, R., Vogel, B., and Wright, J. S.: From ERA-Interim to ERA5: the considerable impact of ECMWF's next-generation reanalysis on Lagrangian transport simulations,
410    Atmospheric Chemistry and Physics, 19, 3097–3124, https://doi.org/10.5194/acp-19-3097-2019, 2019.

Hoffmann, L., Clemens, J., Holke, J., Liu, M., and Mood, K. H.: slcs-jsc/mptrac: v2.2, https://doi.org/10.5281/zenodo.5714528, 2021.

Hoffmann, L., Baumeister, P. F., Cai, Z., Clemens, J., Griessbach, S., Günther, G., Heng, Y., Liu, M., Haghighi Mood, K., Stein, O., Thomas, N., Vogel, B., Wu, X., and Zou, L.: Massive-Parallel Trajectory Calculations version 2.2 (MPTRAC-2.2): Lagrangian transport simulations on graphics processing units (GPUs), Geoscientific Model Development, 15, 2731–2762, https://doi.org/10.5194/gmd-15-2731-2022,
415    2022.

Höpfner, M., Larsen, N., Spang, R., Luo, B. P., Ma, J., Svendsen, S. H., Eckermann, S. D., Knudsen, B., Massoli, P., Cairo, F., Stiller, G., v. Clarmann, T., and Fischer, H.: MIPAS detects Antarctic stratospheric belt of NAT PSCs caused by mountain waves, Atmospheric Chemistry and Physics, 6, 1221–1230, https://doi.org/10.5194/acp-6-1221-2006, 2006.

Höpfner, M., Pitts, M. C., and Poole, L. R.: Comparison between CALIPSO and MIPAS observations of polar stratospheric clouds, Journal
    of Geophysical Research: Atmospheres, 114, https://doi.org/10.1029/2009JD012114, 2009.

Koop, T., Luo, B., Tsias, A., and Peter, T.: Water Activity as the Determinant for Homogeneous Ice Nucleation in Aqueous Solutions, 406,
    611–614, https://doi.org/10.1038/35020537.

Koop, T., Ng, H. P., Molina, L. T., and Molina, M. J.: A New Optical Technique to Study Aerosol Phase Transitions: The Nucleation of Ice
    from H2SO4 Aerosols, The Journal of Physical Chemistry A, 102, 8924–8931, https://doi.org/10.1021/jp9828078, 1998.

Lambert, A., Santee, M. L., Wu, D. L., and Chae, J. H.: A-train CALIOP and MLS observations of early winter Antarctic polar stratospheric
    clouds and nitric acid in 2008, Atmospheric Chemistry and Physics, 12, 2899–2931, https://doi.org/10.5194/acp-12-2899-2012, 2012.

Lambert, A., Santee, M. L., and Livesey, N. J.: Interannual variations of early winter Antarctic polar stratospheric cloud formation and nitric
    acid observed by CALIOP and MLS, Atmospheric Chemistry and Physics, 16, 15 219–15 246, https://doi.org/10.5194/acp-16-15219-
    2016, 2016.

Marti, J. and Mauersberger, K.: A survey and new measurements of ice vapor pressure at temperatures between 170 and 250K, Geophysical
    Research Letters, 20, 363–366, https://doi.org/10.1029/93GL00105, 1993.

Murphy, D. M. and Koop, T.: Review of the vapour pressures of ice and supercooled water for atmospheric applications, Quarterly Journal
    of the Royal Meteorological Society, 131, 1539–1565, https://doi.org/10.1256/qj.04.94, 2005.

Newman, P. A., Nash, E. R., and Rosenfield, J. E.: What controls the temperature of the Arctic stratosphere during the spring?, Journal of
    Geophysical Research: Atmospheres, 106, 19 999–20 010, https://doi.org/10.1029/2000JD000061, 2001.

Noel, V. and Pitts, M.: Gravity wave events from mesoscale simulations, compared to polar stratospheric clouds observed from spaceborne
    lidar over the Antarctic Peninsula, Journal of Geophysical Research: Atmospheres, 117, D11 207, https://doi.org/10.1029/2011JD017318,
    2012.

Orr, A., Hosking, J. S., Delon, A., Hoffmann, L., Spang, R., Moffat-Griffin, T., Keeble, J., Abraham, N. L., and Braesicke, P.: Polar strato-
    spheric clouds initiated by mountain waves in a global chemistry–climate model: a missing piece in fully modelling polar stratospheric
    ozone depletion, Atmospheric Chemistry and Physics, 20, 12 483–12 497, https://doi.org/10.5194/acp-20-12483-2020, 2020.

Pitts, M. C., Poole, L. R., and Gonzalez, R.: Polar stratospheric cloud climatology based on CALIPSO spaceborne lidar measurements from
    2006 to 2017, Atmospheric Chemistry and Physics, 18, 10 881–10 913, https://doi.org/10.5194/acp-18-10881-2018, 2018.

Rivière, E. D., Huret, N., G.-Taupin, F., Renard, J.-B., Pirre, M., Eckermann, S. D., Larsen, N., Deshler, T., Lefèvre, F., Payan, S., and
    Camy-Peyret, C.: Role of lee waves in the formation of solid polar stratospheric clouds: Case studies from February 1997, Journal of
    Geophysical Research: Atmospheres, 105, 6845–6853, https://doi.org/10.1029/1999JD900908, 2000.

Rosenfield, J. E., Newman, P. A., and Schoeberl, M. R.: Computations of diabatic descent in the stratospheric polar vortex, Journal of
    Geophysical Research: Atmospheres, 99, 16 677–16 689, https://doi.org/10.1029/94JD01156, 1994.

Rößler, T., Stein, O., Heng, Y., Baumeister, P., and Hoffmann, L.: Trajectory errors of different numerical integration schemes diag-
    nosed with the MPTRAC advection module driven by ECMWF operational analyses, Geoscientific Model Development, 11, 575–592,
    https://doi.org/10.5194/gmd-11-575-2018, 2018.

Santee, M. L., Tabazadeh, A., Manney, G. L., Fromm, M. D., Bevilacqua, R. M., Waters, J. W., and Jensen, E. J.: A Lagrangian approach to
    studying Arctic polar stratospheric clouds using UARS MLS HNO3 and POAM II aerosol extinction measurements, Journal of Geophys-
    ical Research: Atmospheres, 107, ACH 4–1–ACH 4–13, https://doi.org/10.1029/2000JD000227, 2002.

455  Sembhi, H., Remedios, J., Trent, T., Moore, D. P., Spang, R., Massie, S., and Vernier, J.-P.: MIPAS detection of cloud and aerosol particle occurrence in the UTLS with comparison to HIRDLS and CALIOP, Atmospheric Measurement Techniques, 5, 2537–2553, https://doi.org/10.5194/amt-5-2537-2012, 2012.

Simmons, A., Soci, C., Nicolas, J., Bell, B., Berrisford, P., Dragani, R., Flemming, J., Haimberger, L., Healy, S., Hersbach, H., et al.: Global stratospheric temperature bias and other stratospheric aspects of ERA5 and ERA5. 1, https://doi.org/10.21957/rcxqfmg0, 2020.

460  Solomon, S.: Stratospheric ozone depletion: A review of concepts and history, Reviews of Geophysics, 37, 275–316, https://doi.org/10.1029/1999RG900008, 1999.

Solomon, S., Garcia, R. R., Rowland, F. S., and Wuebbles, D. J.: On the Depletion of Antarctic Ozone, Nature, 321, 755–758, https://doi.org/10.1038/321755a0, 1986.

Spang, R.: MIPAS/Envisat Observations of Polar Stratospheric Clouds, https://doi.org/10.17616/R3BN26, last accessed: 2022-08-22, 2020.

465  Spang, R., Riese, M., and Offermann, D.: CHRISTA-2 observations of the south polar vortex in winter 1997: A new dataset for polar process studies, Geophysical Research Letters, 28, 3159–3162, https://doi.org/10.1029/2000GL012374, 2001.

Spang, R., Remedios, J., and Barkley, M.: Colour indices for the detection and differentiation of cloud types in infra-red limb emission spectra, Advances in Space Research, 33, 1041–1047, https://doi.org/10.1016/S0273-1177(03)00585-4, climate Change Processes in the Stratosphere, Earth-Atmosphere-Ocean Systems, and Oceanographic Processes from Satellite Data, 2004.

470  Spang, R., Arndt, K., Dudhia, A., Höpfner, M., Hoffmann, L., Hurley, J., Grainger, R. G., Griessbach, S., Poulsen, C., Remedios, J. J., Riese, M., Sembhi, H., Siddans, R., Waterfall, A., and Zehner, C.: Fast cloud parameter retrievals of MIPAS/Envisat, Atmospheric Chemistry and Physics, 12, 7135–7164, https://doi.org/10.5194/acp-12-7135-2012, 2012.

Spang, R., Hoffmann, L., Höpfner, M., Griessbach, S., Müller, R., Pitts, M. C., Orr, A. M. W., and Riese, M.: A multi-wavelength classification method for polar stratospheric cloud types using infrared limb spectra, Atmospheric Measurement Techniques, 9, 3619–3639,
475  https://doi.org/10.5194/amt-9-3619-2016, 2016.

Spang, R., Hoffmann, L., Müller, R., Grooß, J.-U., Tritscher, I., Höpfner, M., Pitts, M., Orr, A., and Riese, M.: A climatology of polar stratospheric cloud composition between 2002 and 2012 based on MIPAS/Envisat observations, Atmospheric Chemistry and Physics, 18, 5089–5113, https://doi.org/10.5194/acp-18-5089-2018, 2018.

Stohl, A., Forster, C., Frank, A., Seibert, P., and Wotawa, G.: Technical note: The Lagrangian particle dispersion model FLEXPART version
480  6.2, Atmospheric Chemistry and Physics, 5, 2461–2474, https://doi.org/10.5194/acp-5-2461-2005, 2005.

Tritscher, I., Grooß, J.-U., Spang, R., Pitts, M. C., Poole, L. R., Müller, R., and Riese, M.: Lagrangian simulation of ice particles and resulting dehydration in the polar winter stratosphere, Atmospheric Chemistry and Physics, 19, 543–563, https://doi.org/10.5194/acp-19-543-2019, 2019.

Tritscher, I., Pitts, M. C., Poole, L. R., Alexander, S. P., Cairo, F., Chipperfield, M. P., Grooß, J.-U., Höpfner, M., Lambert, A., Luo, B.,
485  Molleker, S., Orr, A., Salawitch, R., Snels, M., Spang, R., Woiwode, W., and Peter, T.: Polar Stratospheric Clouds: Satellite Observations, Processes, and Role in Ozone Depletion, Reviews of Geophysics, 59, e2020RG000 702, https://doi.org/10.1029/2020RG000702, 2021.

Voigt, C., Schlager, H., Luo, B. P., Dörnbrack, A., Roiger, A., Stock, P., Curtius, J., Vössing, H., Borrmann, S., Davies, S., Konopka, P., Schiller, C., Shur, G., and Peter, T.: Nitric Acid Trihydrate (NAT) formation at low NAT supersaturation in Polar Stratospheric Clouds (PSCs), Atmospheric Chemistry and Physics, 5, 1371–1380, https://doi.org/10.5194/acp-5-1371-2005, 2005.

490  Voigt, C., Dörnbrack, A., Wirth, M., Groß, S. M., Pitts, M. C., Poole, L. R., Baumann, R., Ehard, B., Sinnhuber, B.-M., Woiwode, W., and Oelhaf, H.: Widespread polar stratospheric ice clouds in the 2015–2016 Arctic winter – implications for ice nucleation, Atmospheric Chemistry and Physics, 18, 15 623–15 641, https://doi.org/10.5194/acp-18-15623-2018, 2018.

Waythomas, C. F., Scott, W. E., Prejean, S. G., Schneider, D. J., Izbekov, P., and Nye, C. J.: The 7–8 August 2008 erup-
tion of Kasatochi Volcano, central Aleutian Islands, Alaska, Journal of Geophysical Research: Solid Earth, 115, B00B06,
https://doi.org/10.1029/2010JB007437, 2010.

Weimer, M., Buchmüller, J., Hoffmann, L., Kirner, O., Luo, B., Ruhnke, R., Steiner, M., Tritscher, I., and Braesicke, P.: Mountain-wave-
induced polar stratospheric clouds and their representation in the global chemistry model ICON-ART, Atmospheric Chemistry and Physics,
21, 9515–9543, https://doi.org/10.5194/acp-21-9515-2021, 2021.

WMO: Guide to Instruments and Methods of Observation, WMO-No. 8 (CIMO Guide), Appendix 4B, 2008.

WMO: Scientific Assessment of Ozone Depletion: 2018, Global Ozone Research and Monitoring Project–Report No. 58, Geneva, Switzer-
land, 588 pp., 2018.

WMO: Scientific Assessment of Ozone Depletion: 2022, GAW Report No. 278, Geneva, 520 pp., 2022.

Zhang, J., Tian, W., Chipperfield, M. P., Xie, F., and Huang, J.: Persistent Shift of the Arctic Polar Vortex towards the Eurasian Continent in
Recent Decades, Nature Climate Change, 6, 1094–1099, https://doi.org/10.1038/nclimate3136, 2016.